Reaction of Protonated Tyrosine with Electronically Excited Singlet Molecular Oxygen (a$^1\Delta_g$): An Experimental and Trajectory Study

Yigang Fang and Jianbo Liu*

Department of Chemistry and Biochemistry, Queens College and the Graduate Center of the City University of New York, 65-30 Kissena Blvd., Flushing, New York 11367

Reaction of protonated tyrosine with the lowest electronically excited singlet state of molecular oxygen, $^1O_2$ (a$^1\Delta_g$), is reported over the center-of-mass collision energy (E_{col}) range from 0.1 to 3.0 eV, using an electrospray-ionization, guided-ion-beam scattering instrument, in conjunction with ab initio electronic structure calculations and direct dynamics trajectory simulations. Only one product channel is observed, corresponding to generation of hydrogen peroxide via transfer of two hydrogen atoms from protonated tyrosine. Despite being exoergic, the reaction is in competition with physical quenching of $^1O_2$ and is very inefficient. At low E_{col}, the reaction may be mediated by intermediate complexes and shows strong inhibition by collision energy. At high E_{col}, the reaction efficiency drops to ∼1% and starts to have contribution from a direct mechanism. Quasi-classical trajectory simulations were performed to probe the mechanism at high collision energies. Analysis of trajectories shows that, at E_{col} of 3.0 eV, a small fraction of hydrogen peroxide (25%) is produced via a direct, concerted mechanism where two hydrogen atoms are transferred simultaneously, but most hydrogen peroxide (75%) is formed by dissociation of hydroperoxide intermediates. According to ab initio calculations and trajectory simulations, collisions also lead to formation of various endoperoxides, and dissociation of endoperoxides may play a role in physical quenching of $^1O_2$. The apparatus and experimental techniques are described in detail.

I. Introduction

Oxidation of amino acids with singlet oxygen ($^1O_2$) is an important process associated with biological aging and diseases,[1] photodynamic therapy for cancer treatment,[2] and photochemical transformations in the atmosphere.[3] Because of these biological and photochemical implications, there has been considerable interest in studying these reactions. Most of the experiments are carried out in solution, and the reaction products are identified using chromatographic and spectrophotometric methods. These reactions are often referred to as "photooxidation" because $^1O_2$ is generated with ultraviolet or visible light in the presence of sensitizers[4] (i.e.,

$$\text{sensitizer} \xrightarrow{h\nu} \text{sensitizer*},$$

followed by

$$\text{sensitizer*} \xrightarrow{O_2} \text{sensitizer} + {}^1O_2).$$
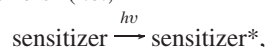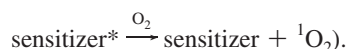
Since other reactive oxygen species (such as O_2^-) may be generated simultaneously during photosensitization and contribute to the reaction, together with various coupled experimental parameters (pH, solvent, temperature, etc.), it is difficult to characterize the reaction intermediates and early products, and to interpret the reaction mechanism.

Tyrosine is one of five amino acids that are most susceptible to oxidative damage by $^1O_2$. It represents important sites of photooxidative damage in proteins. The solution-phase photooxidation rate of tyrosine depends on experimental conditions such as pH, as well as peptide linkages.[5] It was recently proposed[6] that at pH ≤ 7 and in the presence of an α-amino

group (e.g., free Tyr and Tyr-Gly), the reaction proceeds via a ring closure process to form an indolic hydroperoxide intermediate, which subsequently dissociates into the corresponding alcohol. However, in the absence of a free α-amino group (e.g., Gly-Tyr), the cyclization reaction does not occur. Instead, the benzene ring-derived hydroperoxide is formed and slowly decays into alcohol.[6,7]

Here we report a detailed study of ion-excited molecule reaction dynamics for protonated tyrosine (TyrH$^+$) and $^1O_2$ in the gas phase using an electrospray-ionization (ESI)[8,9] guided-ion-beam scattering[10] apparatus. Integral cross sections were measured over a wide range of collision energies (E_{col}). To unravel the reaction mechanism, extensive theoretical approaches were employed. Quantum chemistry calculations were used to find complexes and transition states on the reaction coordinate, then Rice−Ramsperger−Kassel−Marcus (RRKM) theory[11] was used to predict their properties. Finally, direct dynamics trajectory simulations were used to provide additional mechanistic insight.

Many groups are active in studying ion−molecule reactions of amino acids and small peptides, including using ion−molecule reactions as probes of gas-phase structures. One interesting feature of ESI is that it may allow biomolecules to retain their native-like structures when transferred from solution to the gas phase.[12] This makes the native conformations of biomolecules at least metastable in the gas phase.[13] As suggested by Bowers et al.,[14] the dielectric constant of the vacuum ($\varepsilon_{vacuum} = 1$) is close to that of the local environment of biomembranes ($\varepsilon_{peptide/protein} = 2-4$, and $\varepsilon_{lipid} = 2$); thus the gas phase resembles a biomembrane[15] and provides a simplified, yet not unrealistic, model of the membrane environment.[16]

* Author to whom correspondence should be addressed. Electronic mail: jianbo.liu@qc.cuny.edu.
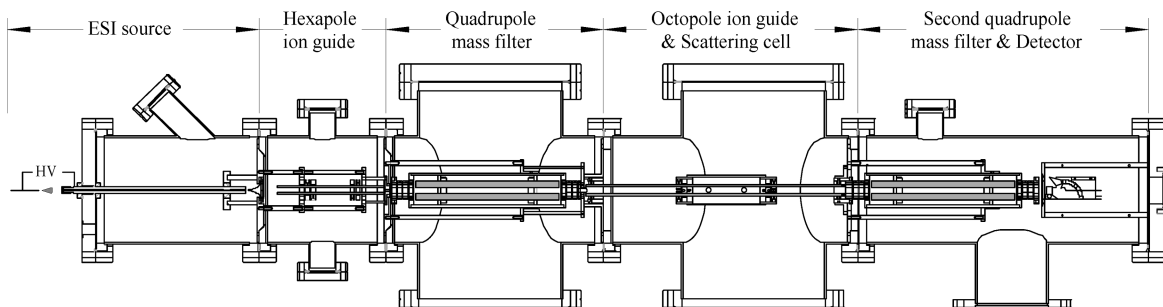
Reaction of Tyrosine with Molecular Oxygen

J. Phys. Chem. A, Vol. 113, No. 42, 2009 **11251**

Figure 1. Schematic diagram of the electrospray-ionization guided-ion-beam mass spectrometer.

II. Experimental Details

A. Instrument and Operating Conditions. A schematic representation of a new ESI, guided-ion-beam tandem mass spectrometer that was used in the present experiment, is shown in Figure 1. The basic concept is similar to guided-ion-beam apparatuses used by other groups.[17−19] Here we describe the instrument in detail, emphasizing the unique features that are pertinent to our specific applications. The apparatus can be divided into five sections: (1) ion source; (2) hexapole ion guide; (3) quadrupole mass filter; (4) octopole ion guide and scattering cell; and (5) second quadrupole mass filter and detector. Briefly, ions are generated in an ESI source, thermalized in a hexapole ion guide and mass-selected using a quadrupole mass filter, and then interact with neutral reactant gas in an octopole ion beam guide. Ionic reactants and products are mass analyzed by a second quadrupole mass filter, and detected.

The sample solution containing tyrosine hydrochloride (MP Biomedicals) is prepared at a concentration of 5×10^{-4} M in HPLC grade methanol and water (1:1 volume ratio). The solution is sprayed into the ambient atmosphere through an electrospray needle using a syringe pump (KdScientific model 100), at a constant flow rate of 0.03 mL/h. The electrospray needle is prepared from 36-gauge hypodermic stainless steel tubing (0.11 mm o.d. × 0.05 mm i.d., Small Parts Inc.), and biased at 3000−3200 V relative to ground. The electrospray needle is mounted on an X-Y-Z stage, so that its position can be adjusted to optimize the ESI performance. The positively charged droplets formed from the electrospray needle are fed into a heated desolvation capillary assembly. The distance between the electrospray needle tip and the capillary entrance is ∼1 cm. The capillary assembly, similar to an arrangement used by Armentrout and co-workers,[18] consists of a stainless steel capillary tubing (1.58 mm o.d. × 0.66 mm i.d. × 25.4 cm long, VICI Precision Sampling Inc.) which fits tightly into a 9.5 mm o.d. × 1.6 mm i.d. stainless steel tubing holder (Higher Pressure Equipment Co.). The assembly is electrically isolated from the front flange using a polyetheretherketone (PEEK) insulator, which allows us to bias the capillary tubing at 100−110 V relative to ground and heat it to 170 °C using heating tape during experiments. Charged liquid droplets and solvated ions undergo continuous desolvation as they pass through the heated capillary,[20] converting to gas-phase ions. Ions are focused toward the capillary axis by the strong gas flow and then transported through the long capillary.[20] The capillary carries ions into the source chamber of the instrument, which is pumped by a 12 L/s rotary pump (Edwards model E2M40) to a pressure of ∼1.8 Torr during experiments.

A skimmer with an orifice diameter of 1.5 mm (Beam Dynamics Inc.) is located 5 mm from the capillary end, separating the first two vacuum regions. The skimmer is biased at 10 V relative to ground, and the electrical field between the capillary and skimmer helps remove remaining solvent molecules attached to ions by collision-induced desolvation[20] and prevent large solvent clusters from depositing downstream.[21,22] Ions that emerge from the skimmer are passed into a hexapole ion guide. The hexapole ion guide is constructed of six 3.18 mm diameter centerless-ground stainless steel rods (PIC Design), 15 cm long, equally spaced on a 9.5 mm diameter circle. Radio frequency (rf) potentials are applied to the rods using a rf generator[23] operating between 2 and 3 MHz with peak-to-peak rf amplitude up to 400 V. The dc bias voltage of the hexapole ion guide is maintained at 1 V. The second vacuum chamber is evacuated by a turbomolecular pump (Varian model V301) backed by a 12 L/s rotary pump (Edwards model RV12). The pumping speed of the turbomolecular pump is adjusted to 70% of its full speed (300 L/s) to keep a pressure of ∼15×10^{-3} Torr in the second chamber. At this pressure range, the mean free path of most ions is around 1−2 mm. Therefore, the interaction of ions with background gas (mainly air and solvent molecules) in the hexapole ion guide leads to collisional focusing, and thermalization of internal and translational energies of ions.[18,24,25] Ions subsequently pass into the third vacuum chamber through an aperture lens, enter a set of entrance focusing lenses followed by a quadrupole mass filter. The quadrupole mass filter uses Extrel 9.5 mm diameter trifilter rods operating at 1.2 MHz (Extrel model 150QC) to cover the mass-to-charge ratio range from 1 to 2000. Mass-selected ions are injected into an octopole ion guide via four focusing lenses, the last of which is held at near-ground potential. The octopole ion guide consists of eight 3.18 mm diameter centerless-ground stainless steel rods, 36.2 cm long, arrayed on a 1.27 cm diameter circle, with rf provided by another rf generator of the same design as that used for the hexapole ion guide. In addition, dc bias voltage is applied to the ion guide, and its amplitude can be varied from −500 to +500 V via an operational power supply (Kepco BOP 500M). The dc bias voltage allows control of the kinetic energy (E_{lab}) of ions in the laboratory frame, thereby setting the collision energy (E_{col}) between ions and reactant gas molecules in the center-of-mass frame, i.e., $E_{col} = E_{lab} \times m_{neutral}/(m_{ion} + m_{neutral})$, where $m_{neutral}$ and m_{ion} are masses of neutral and ionic reactants, respectively. Midway along its length, the octopole is surrounded by a scattering cell. The gas cell is constructed of 3.81 cm i.d. × 11 cm long stainless steel sleeve. To limit its gas conductance, a stainless steel octopole rod holder is attached to each end of the sleeve. The rod holders are isolated from the sleeve with PEEK insulators. Gas is introduced into the cell using stainless steel flexible tubing through a leak valve (Granville Philips model 203). Scattering cell gas pressure is measured by a capacitance manometer (MKS Baratron 690 head and 670 signal conditioner). Both product ions and the remaining reactant ions are collected by the octopole ion guide, extracted by a set of lenses, and mass-analyzed by the second quadrupole
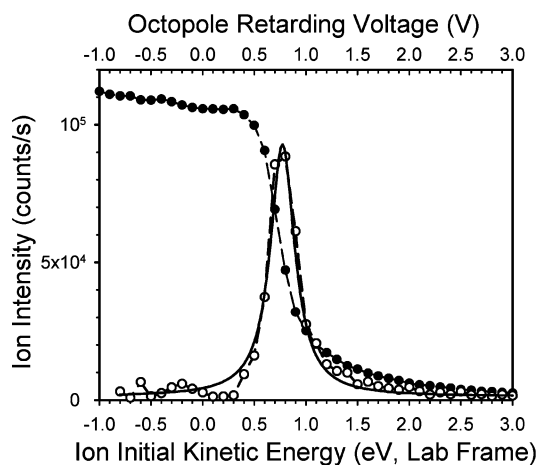
Figure 2. Kinetic energy profile for Na^+(proline), shown in the laboratory frame (lower *x*-axis). Closed circles: ion intensity versus the octopole retarding voltage (upper *x*-axis). Open circles: the first derivative of the retarding potential analysis curve. Solid line: a Lorentzian curve fitted to the data points with a mean of 0.75 eV and a fwhm of 0.31 eV.

mass filter. For this experiment, the second mass filter (Extrel 9.5 mm diameter trifilter rods) is operating at 2.1 MHz, giving a mass-to-charge ratio range from 1 to 500, but with higher ion transmission and better mass resolution. Ions are detected by an off-axis electron multiplier (DeTech model 411) operating in positive-ion pulse counting mode. The random detector counting noise is less than 1 s^{-1}. The third and fourth vacuum chambers are each pumped by a 700 L/s oil diffusion pump (Edwards Diffstak 160/700P), and the detector chamber is pumped by a 300 L/s oil diffusion pump (Edwards Diffstak 100/300P). During experiments, their pressures are typically 1×10^{-7}, 2×10^{-6}, and 1×10^{-7} Torr, respectively.

The detector signal is amplified by a 100 MHz preamplifier/discriminator (Advanced Research Instruments FT-100), and processed using the standard pulse-counting technique. The instrument is interfaced to two National Instruments PCI-6229 multifunction DAQ cards, controlled by LabVIEW[26] programs developed for ion-counting, mass scans, ion kinetic energy calibrations, and cross section measurements, each with graphical display of the data.

The TyrH$^+$ ion beam intensity is typically 10^5 ions/s and constant within 10%. We performed retarding potential analysis (RPA)[27] using the octopole as the retarder (i.e., primary ion beam intensity is measured while sweeping the octopole dc bias). The initial kinetic energy KE_0 of the primary ion beam is determined to be 0.7−0.8 eV with an energy spread of 0.3−0.4 eV, based on Lorentzian fits to the RPA derivative curves. An example kinetic energy profile for Na^+(proline) generated with this source is demonstrated in Figure 2. Because of ion-neutral mass ratio, this corresponds to an energy spread of 0.06 eV in the center-of-mass frame for collisions of TyrH$^+$ with $^1O_2$.

B. Calibration and Analysis. Integral cross sections are calculated from the ratios of reactant and product ion intensities, the scattering cell gas pressure, and the effective length of the scattering cell. To allow subtraction of background from the detector, and from reactions occurring in the ion guide portions outside the scattering cell, all ion signals are measured with the target gas flow directed into the scattering cell ("cell-on"), and also with the same flow directed into the vacuum chamber ("cell-off").[17] Since these two conditions only differ in the gas density inside the scattering cell, the difference in "cell-on" and "cell-off" signals provides the accurate product ion intensities

due to reactions inside the scattering cell. To calibrate the effective length of the scattering cell, we measured the cross section for collision-induced dissociation of Na^+(proline) with Xe, and scaled our results to that of Moision and Armentrout, which was obtained using two different ion sources, a dc discharge/flow tube source[28] and an ESI ion source.[18] The calibration was performed at multiple cell pressures (0.05, 0.10, 0.15, and 0.25 mTorr), and the relative uncertainty in calibration is determined to be 10−15%. However, there may exist some absolute uncertainty due to the possibility of different collection efficiencies for reactant ions (Na^+(proline), $m/z = 138$) and product ions (Na^+, $m/z = 23$). The calibrated effective cell length is close to what was found for a similar guided-ion-beam scattering cells[29] calibrated using $Ar^+ + D_2 \rightarrow ArD^+ + D$.[27] Therefore, the calibration suggests that, in fact, our collection efficiency is at least reasonably uniform for widely spread reactant and product ion masses.

An obvious issue regarding this ESI ion source is the internal energy distribution of the primary ions. Due to thermalization in the hexapole, we expect the internal energy to be approximately thermal. To address this issue, the energy dependence of the CID cross section of Na^+(proline) + Xe was fit using the modified line-of-centers model[29−31]

$$\sigma(E_{col}) = \sigma_0 \frac{(E_{col} + E_{vib} + E_{rot} - E_0)^n}{E_{col}} \quad (1)$$

for $(E_{col} + E_{vib} + E_{rot}) > E_0$, otherwise, $\sigma(E_{col}) = 0$. Here $\sigma(E_{col})$ is the cross section, σ_0 is an energy-independent normalization constant, E_{vib} and E_{rot} are the vibrational and rotational energy of reactant ions, E_0 is the threshold energy, n is a fitting parameter used to adjust the slope of $\sigma(E_{col})$ (equal to 1.0 in the canonical LOC model[32]). To fit experimental data, this model $\sigma(E_{col})$ function is convoluted with the experimental broadening functions, including those from ion beam and target gas velocities and ion rotational and vibrational energies. The fitting was done using the program developed by Anderson and co-worker.[31] Our interest is in probing the distribution of reactant ion vibrational energy. To this end, we used values of E_0 (=1.94 eV) and n (=1.5) determined by Armentrout et al.[18,28] For target xenon atoms, a Maxwell−Boltzmann distribution of velocities at 300 K was used. For Na^+(proline) ions, we used the RPA measured kinetic energy distribution (Figure 2), and assumed a Maxwell−Boltzmann distribution of rotational energy at 300 K, leaving only E_{vib} adjustable (σ_0 is simply a scaling factor, it does not affect the threshold or curvature of the cross section). In the fitting, the vibrational energy distribution is a function of E_{vib_peak},

$$P(E_{vib}) = \frac{(E_{vib})^{1/2} \times \exp(-E_{vib}/2E_{vib\_peak})}{(E_{vib\_peak})^{1/2} \times \exp(-0.5)} \quad (2)$$

where E_{vib_peak} is the most probable vibrational energy of the Boltzmann distribution by summing over the partition function. Vibrational frequencies of Na^+(proline) were calculated at the B3LYP/6-311G** level of theory and scaled by a factor of 0.9613.[33] The model $\sigma(E_{col})$ was run through a Monte Carlo simulation that includes all experimental broadening factors. For each experimental E_{col}, the simulation was repeated for 20000 samples, thereby building up a simulated cross section for comparison with the experiment. Due to the large number of vibrational modes in Na^+(proline), kinetic shifts in the threshold
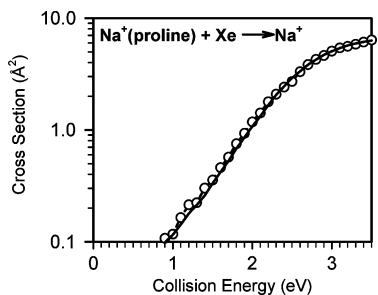
Reaction of Tyrosine with Molecular Oxygen

J. Phys. Chem. A, Vol. 113, No. 42, 2009 **11253**

Figure 3. Cross sections for collision-induced dissociation of Na^+(proline) with xenon as a function of collision energy. Open circles: experimental cross sections. Solid line: simulation based on the modified line-of-centers model.

are expected; i.e., collision energy significantly in excess of the dissociation limit is required to drive fragmentation on the experimental time scale (200−500 μs).[34] To correct for the kinetic shifts, RRKM lifetimes were calculated with the program of Zhu and Hase,[35] assuming orbiting transition states for dissociation. The RRKM results were then used to decide each sample would lead to detectable dissociation or not. The kinetic shift for this system is around 0.15 eV.

Figure 3 shows experimental cross sections for collision-induced dissociation of Na^+(proline) with Xe as a function of E_{col}, together with the corresponding convoluted model $\sigma(E_{col})$ fitted to eq 1. The best fit E_{vib} is around 0.19 eV, which corresponds to a vibrational temperature of 310 K. (For comparison, the average E_{vib} at 298 K is 0.17 eV). The extracted ion vibrational temperature from simulation is slightly elevated from the ambient temperature, presumably due to rf power dissipation by the hexapole. Our conclusion is that primary ions undergo complete thermalization via ion/neutral collisions in the hexapole ion guide and their internal energy can be well-defined using a Maxwell−Boltzmann distribution.

C. Generation of Singlet Molecular Oxygen. One of the unique features of this experiment is the fact that the neutral reactant is an electronically excited state. Singlet molecular oxygen ($a^1\Delta_g$) is generated by microwave discharge[36,37] in a 1:1 mixture of O_2:Ar. The gas flow from the leak valve passes through a 6.3 mm o.d. × 3.0 mm i.d. alumina discharge tube surrounded by an Evenson resonant microwave cavity,[38] which is excited using a 2450 MHz microwave power supply (Opthos Instruments, model MPG-4). The exit end of the discharge tube is coated by mercuric oxide to remove O atoms. The discharge is about 40 cm from the scattering cell entrance, and the light from the discharge is trapped to avoid direct photolysis of the ions or production of background ions by photodesorption from the ion guide surface. When the gas pressure of the scattering cell is 0.35 mTorr, the pressure in the discharge tube is 120 mTorr, and the flow velocity inside the tube is 960 cm/s. The discharge is ignited by a Tesla spark coil (ElectroTechnic Products Inc., model BD-10AS), and the forward microwave power is no more than 20 W. At a pressure of 120 mTorr, it is difficult to obtain a stable discharge of pure oxygen without causing cavity arcing. Adding argon improves the discharge stability. The presence of Ar does not affect the $^1O_2$ reaction measurement, because Ar is unreactive with TyrH$^+$, except for collision-induced dissociation, which can be measured independently. The collision cross section ($\sigma_{collision}$), taken as the greater of the ion-induced dipole capture ($\sigma_{capture}$)[39] and hard sphere cross section ($\sigma_{hard\ sphere}$), is about 40−50 Å^2 for both O_2 + TyrH$^+$ and Ar + TyrH$^+$. $\sigma_{hard\ sphere}$ was calculated from the orientation-averaged contact radii of TyrH$^+$ and O_2 (or Ar), and exceeds $\sigma_{capture}$ for E_{col} > 0.3 eV. The pressure of O_2/Ar in the

scattering cell is maintained at 0.3−0.36 mTorr to provide reasonable signals for the small reaction cross section of the present system, while keeping multiple collision effects to an insignificant level. In this range of pressure, the probability of TyrH$^+$ ions undergoing a single collision is ∼15%, and of double collisions is <3%. The majority of TyrH$^+$ ions (>82%) pass through the scattering cell without any interaction with Ar or O_2. To ensure that the $^1O_2$ yield is constant over our pressure range, a consistency check was performed by measuring cross sections at cell pressure of 0.3 m Torr and 0.36 mTorr, with excellent agreement. Higher or lower cell pressures were not used, to avoid significant multiple collisions or unstable discharge conditions. The discharge cavity is cooled by air blown into the interior of the cavity, and the temperature of the discharge tube is kept below 55 °C. We calculated that the residence time of gas in the discharge is 1−2 ms, and the *specific energy deposition per molecule*[40] (calculated from forward microwave emission power, the power reflected from the cavity, and the density of gas) is 14 eV.

It has been reported that vibrational excitation of O_2 molecules is negligible in microwave discharge as examined by monitoring coherent anti-Stokes Raman scattering from O_2($^3\Sigma_g$);[41] therefore, most O_2($^3\Sigma_g$) molecules are in the vibrational ground state. The absolute concentrations of O_2($a^1\Delta_g$), O_2($b^1\Sigma_g$), and O(^3P) were not determined using emission detection in the present experiment, but such a discharge typically produces 2.5−9% O_2($a^1\Delta_g$), 10^{-3}−10^{-2}% O_2($b^1\Sigma_g$), and 10^{-4}% O(^3P).[42,43] We calculated the deactivation of $^1O_2$ ($a^1\Delta_g$) due to self-quenching and collisional quenching by the wall and gaseous species[44,45] in the downstream tubing. The overall quenching rate is ∼0.05 s^{-1}, and the travel time of $^1O_2$ ($a^1\Delta_g$) downstream is <50 ms; thus the deactivation of $^1O_2$ ($^1\Delta_g$) during its residence time in the system is <0.3%. The quenching of $^1O_2$($b^1\Sigma_g^+$) is spin-allowed and thus is ∼10^5 times more efficient than that of $^1O_2$ ($a^1\Delta_g$).[36] The lifetime of O atoms with respect to recombination is in the range of milliseconds under the conditions of our inlet line,[41] and therefore, any O atoms not removed by collision with mercuric oxide would decay along the gas line. We measured the mass spectra of the background gas in the octopole chamber using an electron impact ionization source, and found no increase of O$^+$ intensity when the microwave discharge lights.

To check the reactivity of TyrH$^+$ toward ground state O_2 and Ar, we run the experiments with ground state O_2, and with pure Ar (with the discharge on and off) at the same total cell pressure. Because the cross section we are measuring for reaction of TyrH$^+$ and $^1O_2$ is small, it is important to minimize systematic variation in experimental conditions that might be caused by drifting potentials, changes in ion beam intensities, $^1O_2$ yield, etc. In the experiments, we cycled through the different collision energies several times. The RPA measurements of primary ions were performed before and after each experiment to check the initial kinetic energy of the primary ion beam. The entire experiment was repeated several times to check the reproducibility. On the basis of the reproducibility of the cross section measurements taken over a 3 week period, we estimate that the relative error is <20%.

III. Computational Details

To aid in reaction coordinate interpretation, ab initio calculations were performed at the B3LYP/6-21G and B3LYP/6-31+G* levels of theory, using Gaussian 03 (C.01).[46] Geometries were optimized by calculating the force constants at every step. Vibrational frequencies and zero-point energies were scaled by a factor of 0.9613 and 0.9804,[33] respectively. All the transition

states (TS) found were verified to be first-order saddle points by frequency calculations. RRKM rates and density of states were done with the program of Zhu and Hase,[35] using its direct count algorithm, and scaled frequencies and energetics from the ab initio calculations.

Quasi-classical, direct dynamics trajectories were calculated using the chemical dynamics program VENUS99 of Hase et al.[47] to set up the trajectory initial conditions, and the Hessian-based method of Bakken et al.[48] implemented in Gaussian 03(C.01) to propagate each trajectory, with Hessians recalculated every five steps. The integrations were performed with a step size of 0.25 amu$^{1/2}$ bohr ($\sim$0.4 fs), which conserved total energy to better than 10^{-4} Hartree. The SCF = XQC option was used during trajectory integration so that a quadratically convergent Hartree−Fock (QC-SCF) method[46,49] was used in case the usual, but much faster, first-order SCF method did not converge within the allotted number of cycles.

Because millions of gradients and Hessian evaluations were required, the level of ab initio theory used was necessarily modest. To select a suitable level of theory, we performed relaxed potential energy surface (PES) scans for approach of $^1O_2$ to TyrH$^+$ in several orientations with various basis sets (including MP2/6-21G, MP2/6-31G, B3LYP/3-21G, B3LYP/6-21G, and B3LYP/6-31G). We then compared these results to benchmark calculations, consisting of single-point calculations at the geometries sampled in the relaxed PES scans, using B3LYP/6-311++G** and QCISD/cc-pVDZ levels of theory. Unfortunately, MP2 methods run into convergence problems for this system. For all B3LYP methods, the $^1O_2$−TyrH$^+$ surface has a broad, electrostatic well at long-range (2.3−3.3 Å center-of-mass separation) and then a barrier peaking at 1.8 Å separation, before a drop into a complex well. The shapes of the attractive wells are in reasonable agreement for B3LYP methods with different basis sets, the principle difference being that the well is deeper at smaller basis sets. On the basis of the overall level of agreement and computational speed, we chose the B3LYP/6-21G level of theory for the main set of trajectories.

The initial conditions for the trajectories were chosen to mimic the conditions of our experiment. Because TyrH$^+$ ions are thermalized in the experiment, their initial vibrational and rotational energies were sampled from Boltzmann distributions at 300 K. Similarly, $^1O_2$ in the experiments was close to room temperature, so 300 K was used for both rotational and vibrational temperature. The quasi-classical initial vibrational state is simulated by giving each reactant atom displacement from equilibrium and momentum appropriate to the initial rovibrational state, with random phases for the different modes. Both TyrH$^+$ and $^1O_2$ have zero-point energy (ZPE) in all vibrational modes. Trajectories were calculated for the collision energy of 3.0 eV. A few trajectories were also tried for low E_{col}; however, the collision time scale was far too long for practical trajectory simulations.

Batches of trajectories (125 each) were calculated for discrete values of the reactant impact parameter (b = 0.1, 0.5, 1.0, 1.5, 2.0, 2.5, 3.0, and 4.0 Å) rather than randomly sampling the b distribution. In addition, the random number generator seeds used in setting up initial conditions for each batch of trajectories were identical.[50,51] Each trajectory batch, therefore, used the same pseudorandom sequence to sample the reactant parameters (orientations, rotational and vibrational energies, vibrational phases, etc.). As a result, it is easy to compare trajectories for different impact parameters, because corresponding trajectories from different batches have identical initial conditions, except for the impact parameter being varied. The error from inadequate

sampling of reactant parameter space is the same for all batches, and tends to cancel when comparing batches for different impact parameters.

All trajectories started with an initial center-of-mass reactant separation of 9.0 Å, and were terminated either when the distance between the final products exceeded 9.0 Å, or after 2000 steps. The error in the energy due to the long-range potential at 9 Å is less than 7 meV. Approximate one thousand trajectories were calculated, each taking $\sim$260 CPU hours on an Intel dual-core based cluster. For trajectory visualization we used the program gOpenMol.[52] Detailed analysis of individual trajectories and statistical analysis of the trajectory ensemble was done with programs written for this purpose.[50,53−55]
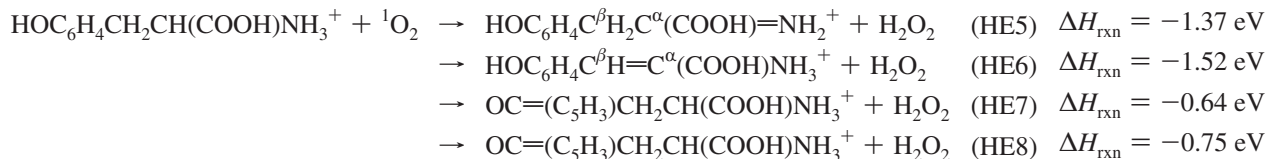
One obvious issue with using the QCT method to probe dynamics is that vibrational energy is not quantized. At the start of the trajectories, vibrational energy is partitioned appropriately to represent the initial internal temperature. Lack of quantization allows unphysical distribution of energy between vibrational modes during and after collisions,[56,57] including having trajectories where the final E_{vib}' is below the zero point level. Because we are working at high collision energies, such obviously unphysical behavior is not observed in our trajectories. We note that the purpose of our trajectory simulations is to probe the gross features of the reaction mechanism, particularly at early times in the collisions; thus errors from classical treatment of the nuclear motions should be minimal.

IV. Results and Discussion

A. Integral Cross Section. For TyrH$^+$ (m/z 182) + $^1O_2$, product ions are observed at m/z 180 over the collision energy range 0.1−3 eV. At high collision energies, product ions are also observed at m/z 165 and 136, even when the O_2 microwave discharge is off. Products with m/z 165 and 136 correspond to the elimination of NH$_3$ and of (H$_2$O + CO), respectively, from TyrH$^+$, and are attributed to collision-induced dissociation.[58−60] Product ions of m/z 180, which are not observed with Ar or ground state O_2, correspond to the transfer of two hydrogen atoms from TyrH$^+$ to form H$_2$O$_2$ (referred to as **H2T** channel). There are four possible routes leading to the H2T channel as shown below and the product structures are given in Figure 6. The energetics are derived from B3LYP/6-31+G* calculations. In principle, the m/z 180 product ions could also be due to the elimination of H$_2$ by collision-induced dissociation of TyrH$^+$. However, we can discount this channel, except perhaps at high energies, because it is calculated to be at least 1.1 eV endoergic.

As discussed above, the concentrations of O and O$_2$(b$^1\Sigma_g$) in the scattering cell are negligible. O$_3$ is another species that potentially could be produced in the discharge or during quenching of $^1O_2$.[40] O$_3$ can react with TyrH$^+$, and the main ozonation product is dihydroxyl phenylalanine formed by addition of one oxygen atom.[61,62] Because no (TyrH + O)$^+$ (m/z 198) ion is observed, we conclude that the ozone concentration is also negligible, and therefore, that H$_2$O$_2$ is a product from the reaction with $^1O_2$.

Production of H$_2$O$_2$ from reaction of TyrH$^+$ with $^1O_2$ is surprising and has not been reported in solution-phase photo-oxidation. In fact, despite the significant body of work probing $^1O_2$ chemistry, there is little known about production of H$_2$O$_2$ from $^1O_2$ reactions with biomolecules. We are aware of only a few previous studies looking at production of H$_2$O$_2$ from $^1O_2$-mediated oxidation. One was the reaction of $^1O_2$ and ascorbate in solution, reported by Buettner et al.[63] Subsequently the same group reported a 1:1 stoichiometry and proposed a hydroper-oxide intermediate.[64] Antibodies could generate H$_2$O$_2$ from $^1O_2$,

Reaction of Tyrosine with Molecular Oxygen

J. Phys. Chem. A, Vol. 113, No. 42, 2009 **11255**

$$HOC_6H_4CH_2CH(COOH)NH_3^+ + {}^1O_2 \rightarrow HOC_6H_4C^{\beta}H_2C^{\alpha}(COOH)=NH_2^+ + H_2O_2 \quad (HE5) \quad \Delta H_{rxn} = -1.37 \text{ eV}$$

$$\rightarrow HOC_6H_4C^{\beta}H=C^{\alpha}(COOH)NH_3^+ + H_2O_2 \quad (HE6) \quad \Delta H_{rxn} = -1.52 \text{ eV}$$

$$\rightarrow OC=(C_5H_3)CH_2CH(COOH)NH_3^+ + H_2O_2 \quad (HE7) \quad \Delta H_{rxn} = -0.64 \text{ eV}$$

$$\rightarrow OC=(C_5H_3)CH_2CH(COOH)NH_3^+ + H_2O_2 \quad (HE8) \quad \Delta H_{rxn} = -0.75 \text{ eV}$$

and the process is catalytic.[65] It is interesting to note that antibodies harbor tyrosine, although in that paper tyrosine is interpreted as a photosensitizer for ${}^1O_2$ generation. More recently, Eyte et al. reported production of H_2O_2 in the reactions of ${}^1O_2$ with $C_2H_5O^-$ and $(CH_3)_2CHO^-$.[66] The biological implication of these reactions is that locally produced ${}^1O_2$ with a short lifetime changes to H_2O_2 that has much longer lifetime and can diffuse to distant targets in biological systems.

We will focus the rest of our discussion on the **H2T** channel, producing H_2O_2 from ${}^1O_2$. The integral cross section for the H2T channel is given in Figure 4, over the E_{col} range from 0.1 to 3.0 eV, in the center-of-mass frame. Note that the absolute values of cross sections were calculated using a 5% ${}^1O_2$ yield (${}^1O_2$%) in the microwave discharge. We obtained the value of ${}^1O_2$% on the basis of the *specific energy deposition per molecule* in the discharge. The correlation between ${}^1O_2$% and specific energy deposition in O_2 molecules is independent of the discharge type. In the present experiment, the specific energy deposition is 14 eV per molecule, which corresponds to a 5% ${}^1O_2$ yield.[40] Our calculated ${}^1O_2$ yield is well within the reported range of 2.5–9% under similar microwave discharge conditions, measured using ${}^1O_2$ emission detection schemes.[42,43]

We state that the absolute uncertainty in the cross section, arising largely from uncertainty in the ${}^1O_2$ concentration, could be as large as a factor of 2. This source of uncertainty does not affect the relative cross section, i.e., the collision energy dependence, which is our primary interest here. The relative uncertainty is estimated to be ∼20%. The reaction is strongly suppressed by collision energy at low E_{col}, becoming energy independent at $E_{col} > 1.0$ eV. Note that the various CID channels do not interfere with H_2O_2 production at low E_{col}, because they have thresholds estimated to be between 1.1 and 1.7–1.8 eV (calculated at B3LYP/6-31+G**).[67] The nearly energy-independent cross section above ∼1 eV may include a contribution from the H_2 elimination CID channel, which is ∼1.1 eV endoergic. There is a decrease of the cross section at our lowest E_{col}. Since heavy ion/light neutral kinematics for the present system is expected to result in a good collection efficiency for product ions at low E_{col}, a dip of cross section suggests that there may be a bottleneck or barrier, or another channel overwhelms and shuts down the H2T channel.

Based on the estimated cross section values, the reaction efficiency (=$\sigma_{reaction}/\sigma_{collision}$) is only ∼3% at $E_{col} = 0.2$ eV, drops to 2.5% at $E_{col} = 0.5$ eV, and drops to less than 1% at E_{col} above 1.0 eV. One interesting mechanistic question is why the reaction efficiency is so low, despite the fact that the reaction is exothermic. The extremely low efficiency may reflect interchannel competition between the chemical reaction and physical quenching of ${}^1O_2$.

B. Reaction at Low Collision Energies.

1. Reaction Coordinate. One issue for interpretation of amino acid chemistry is that amino acids exist in various geometric conformations resulting from the flexibility of their structures. The α-amino nitrogen is the preferred protonation site for tyrosine.[68] Considering all possible conformations, 3 orientations for the $C^{\alpha}-C^{\beta}$ bond, 2 for −COOH, 2 for carboxyl −OH, and 2 for phenolic −OH, a total of 24 conformations are expected for TyrH$^+$. Eighteen of these are found to be stable at B3LYP/

6-31+G* level of theory. Their structures and relative energies (with respect to 2B, the lowest energy conformation at B3LYP/6-31+G*) are summarized in Figure 5. Each structure represents a pair of conformers, corresponding to two different orientations of the phenolic −OH on the ring, with small energy differences (within 10 meV). This is consistent with those found for neutral tyrosine.[69] Calculations of the reaction coordinate were focused on one of the most stable conformations, 1A in Figure 5. (1A is the lowest energy conformation at the level of B3LYP/6-21G which we used for trajectory simulations.) It is certainly possible that interconversion between various conformations might occur in the course of reaction. It seems unlikely, however, that different conformations would significantly change the reaction coordinate, and our trajectory calculations confirm this conclusion.

Ab initio computational results for the reaction coordinate of TyrH$^+$ + ${}^1O_2$ are summarized in Figure 6, with the reactants shown near the center at zero energy. The energies are from a combination of B3LYP/6-21G and B3LYP/6-31+G* calculations. Eight weakly bound complexes (C1−C8) and eight covalently bound complexes (including six endoperoxides and two hydroperoxides) were found. We attempted to locate transition states (TSs) connecting the complexes to reactants and products, and those found are indicated in Figure 6. The details of the geometries for these complexes, TSs, and products are available upon request to the corresponding author. C1−C4 can be characterized as reactant-like, electrostatically bound complexes. All four complexes have O_2 oriented parallel to the phenol ring, with the closest distances between O_2 and the phenol ring being 1.9−2.4 Å. The affected carbon atoms are slightly displaced from the ring plane toward O_2. The binding energies are ∼1.2 eV (with respect to reactants) for C1 and C2, and ∼0.3 eV for C3 and C4. C1 and C2 are more stable than C3 and C4, because of the hydrogen bonding between amino hydrogen and O_2. C5−C8 are hydrogen-bonded complexes. C5 has both −C$^{\alpha}$H and −NH$_3$ hydrogen atoms bonded to O_2 moiety with H···O distances of 1.8−2.3 Å. C6 has the hydrogen bonds formed between −C$^{\alpha}$HC$^{\beta}$H$_2$ and O_2 with H···O distances of 1.8−2.5 Å. C7 and C8 have hydrogen bonds between phenol H and O_2 moiety with H···O distances of 1.8 Å. The binding energies of C5 and C6 are ∼0.5 eV with respect to the reactants, and those of C7 and C8 are −0.72 eV. Presumably, C1 and C2, C3 and C4, and C5 and C6 can interconvert rapidly. Because no rearrangement is required to form all these reactant-like complexes, it is unlikely that there would be significant activation barriers inhibiting their formation.

Bicyclic endoperoxides (E1A/B, E2, E3A/B, and E4) and hydroperoxides (H7 and H8) are covalently bound intermediates. Endoperoxides can be grouped on the basis of their orientations. Endoperoxides E1A/B and E2, converted from weak complexes C1 and C2 via TS1A/1B and TS2, have oxygen atoms bonded to two *para*-C atoms of the phenol ring with the backbone bent toward O_2. Endoperoxides E3A/B and E4, are analogues to E1A/B and E2, except that the backbone is bent away from O_2. For E1A/B and E3, the hydrogen bonds between amino hydrogen and O_2 moiety help stabilize the structures. Consequently, the energies of E1A/B and E2 are lower by 1 eV compared to those of E3A/B and E4. Hydroperoxides H7 and
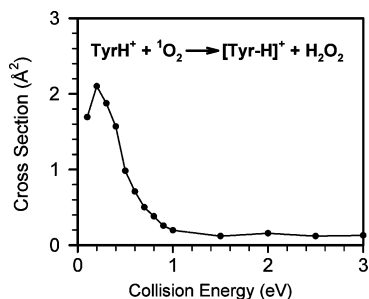
Fang and Liu

Figure 4. Cross sections for production of H_2O_2 from the reaction of protonated tyrosine with $^1O_2$, as a function of collision energy.
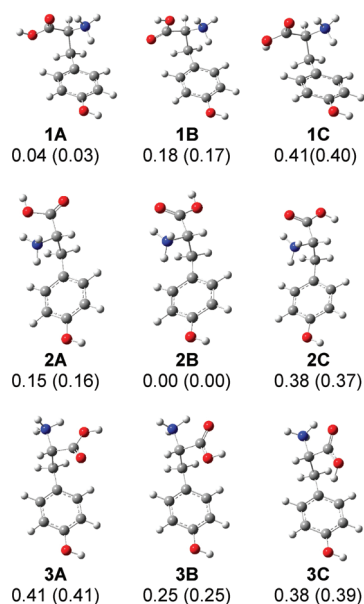

Figure 5. Different conformations of protonated tyrosine calculated at B3LYP/6-31+G*, and their energies relative to **2B** (indicated below each structure, in eV). Note that the rotation of the phenolic −OH results in a pair of stable conformations, only one of which is illustrated, and the energy of the other is given in parentheses.

H8 (both of which were observed in the trajectory simulations) are converted from C7 and C8, via an ene reaction with abstraction of the phenolic H atom. In the solution, the oxidation of *para*-alkylphenol with $^1O_2$ results in *para*-hydroperoxyquinols.[70] However, this structure is not observed in our direct trajectory simulations. Note that the nascent endoperoxides and hydroperoxides have high internal energies. Various fragmentation pathways of these complexes can be expected, such as dissociation back to reactants, elimination of H_2O_2, or decay to ground state $^3O_2$.

The calculations suggest possible pathways leading to H2T products at low collision energies. Hydroperoxides H7 and H8 can eliminate H_2O_2 to give the corresponding H2T products. Elimination of H_2O_2 is common for allylic hydroperoxides in the presence of a labile hydrogen on a neighboring atom.[71,72] More recently, Davies et al. reported production of H_2O_2 from collision-induced dissociation of hydroperoxide products generated from sensitized photooxidation of tryptophan, valine and leucine.[72,73] The structures of H2T product ions could not be determined by the present experiment, and the structures of HE7 and HE8 in Figure 6 are from ab initio calculations (we took off an H_2O_2 moiety and used the remaining structures of the hydroperoxides as the initial structures for geometry optimizations). We also ran trajectory simulations for hydroperoxides for several picoseconds at HF/3-21G, with randomly distributed

internal energy equivalent to what the complex would have in reaction. During the trajectory time, the benzene ring breaks between C−OOH and C−O, which supports the calculated structures of HE7 and HE8. The heats of reaction (ΔH_{rxn}) for HE7 and HE8, are calculated to be −0.64 and −0.75 eV, respectively. We were not able to locate the transition states from H7 and H8 to HE7 and HE8 but would not expect activation barriers above the reactant energy for H_2O_2 elimination. Complexes C5 and C6 might act as intermediates for direct H2T. Two low energy pathways are found linking C5 and C6 to H2T products, either transferring two H atoms from −C$^\alpha$H and −NH$_3$ of C5 (via TS5), or transferring two H from −C$^\alpha$H and −C$^\beta$H$_2$ of C6 (via TS6). ΔH_{rxn} values for corresponding products HE5 and HE6 are −1.37 and −1.52 eV, respectively. However, there are higher energy barriers associated with these two channels (+0.17 eV for TS5 and −0.13 eV for TS6). We cannot exclude the existence of some additional reaction pathway(s) leading to H_2O_2 but conclude that the pathways included in Figure 6 are certainly important.

2. Complex-Mediated Mechanism? To evaluate whether the complexes and reaction paths identified in ab initio calculations can account for the experimental observation, we have to calculate the reaction efficiency expected from statistical decay of the intermediate complexes. We first used the ratio of the density of states (DOS) in these complexes[74] to determine the relative formation efficiencies so that we can determine which complexes might have significant contributions to the "statistical" reaction. The DOS would also determine the importance of each structure if interconversion between complexes is facile. The DOS is energy dependent, and it turns out that at low E_{col} only complexes C1, C2, C7, and C8 are important. Complexes C3−C6 have high energies and low DOS, making their contributions negligible. For this reason, only C1, C2, C7, and C8 are considered further. The DOS ratios for (C1 + C2):(C7 + C8) are 97.5:2.5 at E_{col} = 0.1 eV, 96:4 at E_{col} = 0.2 eV, and 95:5 at E_{col} = 0.5 eV.

Besides formation efficiency, the mechanistic importance of the complexes depends on their lifetimes and decomposition branching. We calculated RRKM rates for decomposition of each complex for all decomposition channels indicated by dashed lines in Figure 6. No barriers are expected for decay of these complexes "back to reactants"; thus orbiting transition states[34] have been assumed. The orbital angular momentum L was estimated from the collision cross sections, i.e., $L = \mu \cdot v_{rel} \cdot (\sigma_{collision}/\pi)^{1/2}$, where μ and v_{rel} are the reduced mass and relative velocity of collision, respectively. At low collision energies ($E_{col} < 0.5$ eV), these complexes have lifetimes ≥10 ps. For comparison, the classical rotational period of the complex estimated using the average angular momentum is 7 ps at E_{col} = 0.1 eV, decreasing to 4 ps at E_{col} = 0.5 eV. We also estimated the direct reaction time, taken as the time required for 5 Å motion at the relative speed of the reactants. This gives a measure of how long a direct collision would last at the same collision energy. This "fly by" time ranges from 0.6 psec at E_{col} = 0.1 eV to 0.27 ps at E_{col} = 0.5 eV. The complex lifetimes are, thus, significantly longer than the "fly by" times, and comparable to the complex rotational periods.

However, the existence of suitable complexes does not mean that the mechanism is necessarily complex-mediated. A better test is to compare the experimental and RRKM predicted reaction efficiency. RRKM calculations predict that the dominant decay channel for C1 and C2 corresponds to forming endoperoxides, with negligible branching back to reactants (<0.1%). At low E_{col} the dominant decay channel for C7 and C8
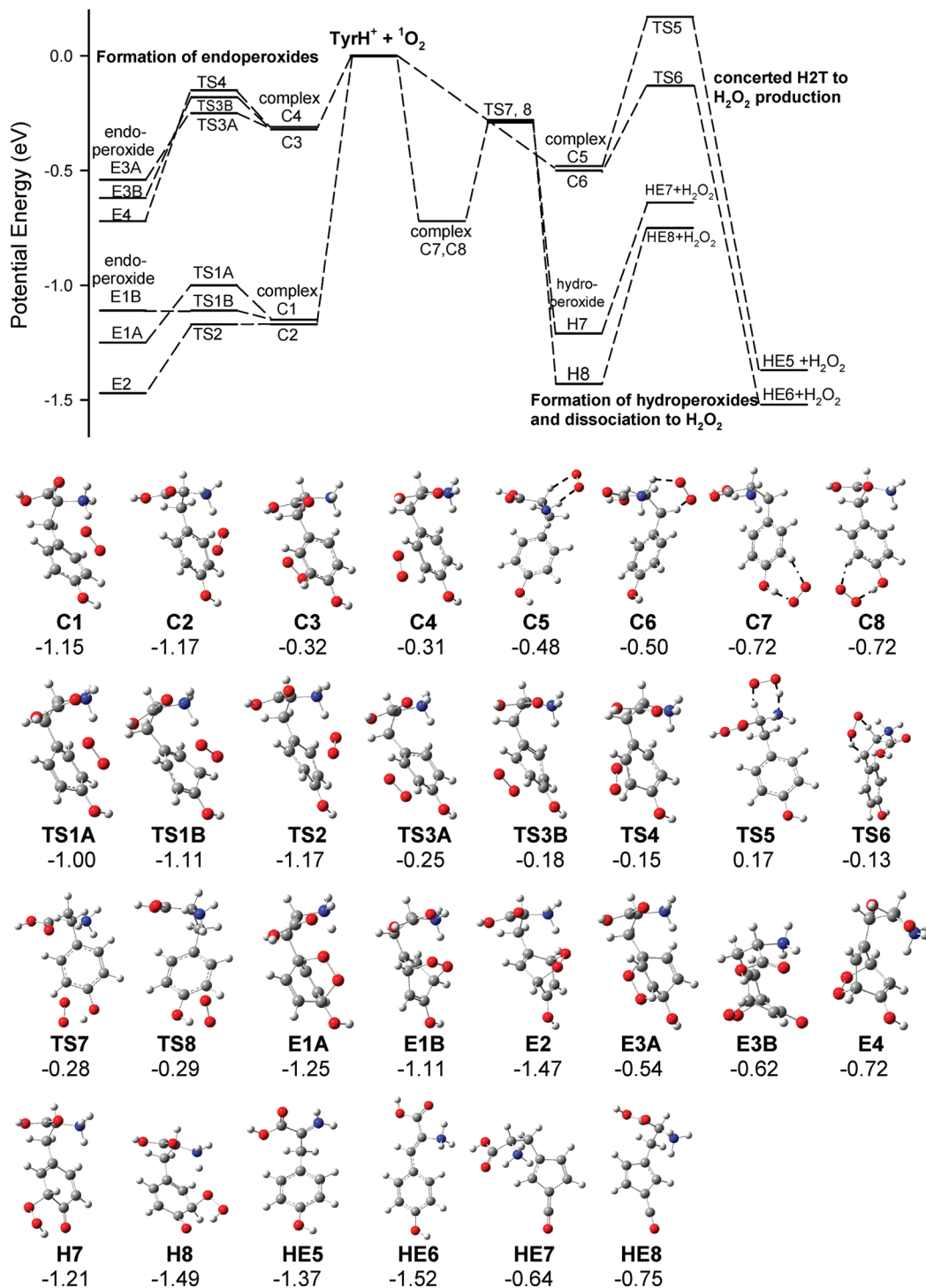
Reaction of Tyrosine with Molecular Oxygen

J. Phys. Chem. A, Vol. 113, No. 42, 2009 **11257**

Figure 6. Schematic reaction coordinate for protonated tyrosine and $^1O_2$. Energies of complexes, TSs, and products, relative to reactants, are indicated (in eV) below each structure. Energies are derived from a combination of B3LYP/6-21G and B3LYP/6-31+G* values, including zero point energies. For H2T products (HE5−HE8), the energies include that of H_2O_2.

correspond to forming hydroperoxides. The branching between decay of C7 and C8 to hydroperoxides and "back to reactants" is 80:20 at E_{col} = 0.1 eV, decreasing to 60:40 at E_{col} = 0.2 eV and 10:90 at E_{col} = 0.5 eV. Assuming the dominant decay pathway for hydroperoxides is to H2T, the net reaction efficiency for H2T is the product of the probability of trapping into C7 and C8 and the branching ratio to hydroperoxides. The RRKM reaction efficiencies for H2T are estimated to be 2% at E_{col} = 0.1 eV, 2.4% at E_{col} = 0.2 eV, and 0.5% at E_{col} = 0.5 eV. Taking the collision cross section as an upper limit for complex formation, we can estimate the complex-mediated contribution

to H2T is 1.5 Å^2 at E_{col} = 0.1 eV, 1.7 Å^2 at E_{col} = 0.2 eV, and 0.2 Å^2 at E_{col} = 0.5 eV. For E_{col} up to 0.2 eV, therefore, the estimated complex contribution to the H2T cross section is close to the experimental measured cross sections. The complex-mediated model also reproduces the decrease of cross section at lowest E_{col}. This suggests that complex mediation may be important at our lowest energies. Note, however, that RRKM predicates a much faster decrease of the cross sections with increasing E_{col} than is observed experimentally. For example, at E_{col} = 0.5 eV, the experimental H2T cross section is about 5 times larger than the RRKM predicted value, suggesting that

11258 *J. Phys. Chem. A, Vol. 113, No. 42, 2009*

Fang and Liu

complex mediation is a minor mechanism for energies above a few tenths of an electronvolt.

The observation of low reaction efficiency is consistent with solution-phase results. According to solution-phase experiments, photooxidation of tyrosine by $^1O_2$ is pH dependent.[75–78] Chemical quenching of $^1O_2$ by tyrosine is only observed in basic solution, when the dissociated phenolate group is present.[6,79] In acidic solution when the phenolic group is in the molecular form, quenching of $^1O_2$ is merely a physical process. Chemical quenching only accounts for <1% of total quenching. As discussed above, the complex-mediated model predicts formation of various endoperoxides with efficiency over 90%. This raises two closely related questions: Can endoperoxides decay back to reactants? Can endoperoxides act as intermediates for physical quenching of $^1O_2$? Both questions hinge on the properties of endoperoxides and will be discussed below.

C. Reaction at High Collision Energies.

1. Nature of the Trajectories at $E_{col} = 3.0$ eV. Trajectory calculations were run for $E_{col} = 3.0$ eV. Roughly 90% of all trajectories are characterized as direct, nonreactive scattering, resulting in conversion of some collision energy into vibrational and rotational energy (T → $E_{internal}$ conversion). The H2T trajectories can be grouped into two classes, either via direct, concerted H2 transfer (~2% of total trajectories) or by forming hydroperoxides H7 and H8 (~4%). The latter are assumed to eventually decay to H2T products based on the RRKM branching discussed above, but it is not practical to propagate the trajectories long enough to observe this decay. The remaining trajectories (4%) form a mixture of endoperoxides.

Trajectories representative of two H2T mechanisms are illustrated in Figure 7a,b, both showing changes of various distances and the potential energy (PE) during the trajectory. The CM distance is the distance between the centers of mass of the collision partners, and in Figure 7a the two r_{CH} and r_{OH} distances correspond to the two C–H bonds being broken, and the two H–O bonds being formed in the reaction. The oscillation in the bond lengths and PE reflects the vibrations of the reactants and products, including ZPE. Figure 7a shows a direct H2T trajectory, with only one turning point in the relative motion of the reactant centers of mass; i.e., there is no sign of mediation by a complex in this collision. The time for reactant approach is ~120 fs, and the time during which the interaction is strong is ~50 fs. We note that actual transfer of two H atoms, defined as the time point where the CH bonds of tyrosine extends by more than 2 times the normal amplitude, occurs right after the CM turning point. Note also that the H2T reaction is concerted; i.e., the two CH bonds break simultaneously, and the two OH bond form at the same time.

Figure 7b shows the formation of a hydroperoxide, with a similar reactant approach time. No dissociation was observed for the hydroperoxide during the trajectory time (800 fs). It is interesting to note that of the hydroperoxides formed in trajectories, 75% have the structure of H8, and 25% have the structure of H7, because the latter involves the rotation of phenolic –OH in TyrH$^+$.

Direct H2T reaction is observed only in trajectories where the collision geometry allows the simultaneous rupture of two C–H (or C–H and N–H) bonds in tyrosine while forming the two O–H bonds in H$_2$O$_2$, as shown in Figure 7a. Such a complicated process can occur only in collisions with "O$_2$ in parallel to the two H atoms being transferred", i.e., with collision geometries similar to those of C5 or C6 in Figure 6. Since direct H$_2$ transfer occurs very close to the center-of-mass turning points, we examined the correlation between reaction probability
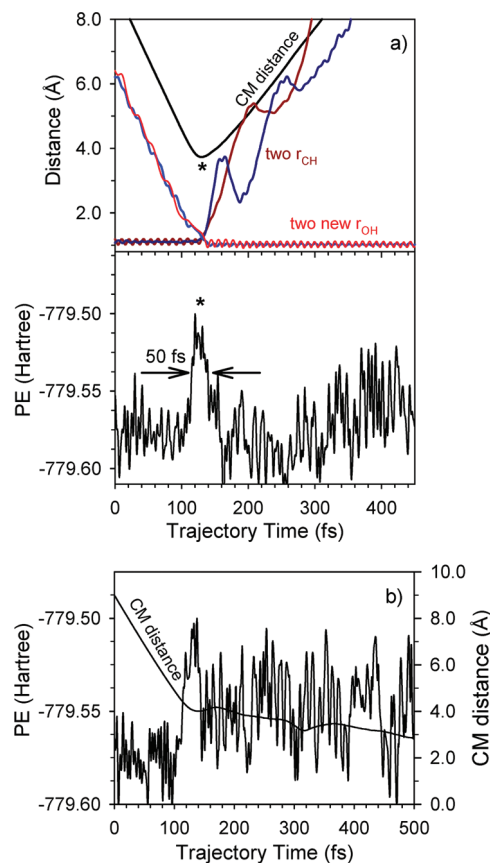

Figure 7. Representative plots of H2T trajectories: (a) direct H2T trajectory; (b) hydroperoxide-forming trajectory. Plots show the variation of various bond lengths, center-of-mass distances, and potential energies during the trajectories.

and reactant orientation at the center-of-mass turning points for each collision. Typically, for impact parameters less than 2.0 Å, only ~8% of collisions have favorable reactant orientations at their center-of-mass turning points, and of these only 10% actually lead to H$_2$ transfer.

Most hydroperoxide-forming trajectories have O$_2$ close to the phenolic group of TyrH$^+$, and the chance of having such orientation at the time when reactants start to collide is only ~13%, out of these collisions ~30% form hydroperoxides. Therefore, at high collision energies, the reaction efficiency is mostly controlled by the reactant impact parameter and collision orientation.

2. Trajectory Reaction Cross Section. Because trajectories were calculated at discrete b values, the trajectory cross sections were estimated using an extended closed trapezoidal approximation[80] to the usual integral form (eq 3), where $P(b)$ is the fraction of reactive trajectories at each impact parameter, i.e., the opacity function.

$$\sigma = 2\pi \int_0^{b_{max}} P(b)b \, db \approx \pi \sum_{b_i=0}^{b_{max}} [P(b_i) \times b_i + P(b_{i+1}) \times b_{i+1}] \times (b_{i+1} - b_i) \quad (3)$$

The trajectory opacity functions are given in Figure 8. The error limits given for $P(b)$ are statistical, based on the number of total trajectories and reactive trajectories for each impact parameter, and obviously do not include any systemic errors. We lump the direct H2T and hydroperoxide channels to calculate H2T
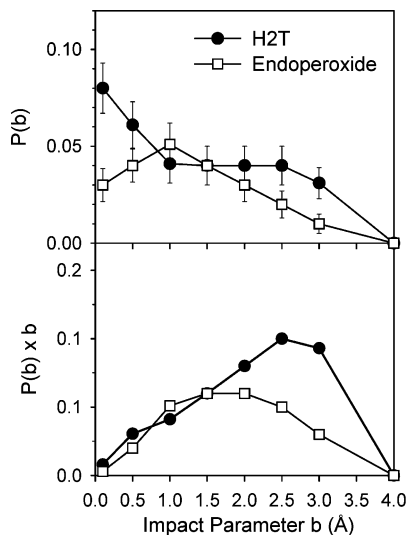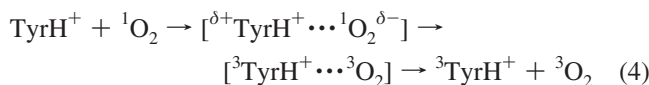
Reaction of Tyrosine with Molecular Oxygen

J. Phys. Chem. A, Vol. 113, No. 42, 2009 **11259**

Figure 8. Opacity functions for H2T reaction and formation of endoperoxides.

opacity functions. Also shown in Figure 8 are b-weighted opacity functions $P(b) \times b$'s (i.e., the contribution of each range of b to the reaction cross section). For both H2T and endoperoxide channels, $P(b)$s decrease at large b. The maximum b at which reactions are observed is 2.0 Å for direct H2T, and 3.5 Å for hydroperoxides and endoperoxides. The values of b_{max} are close to the orientation-averaged hard-sphere collision radius of 3.8 Å. Because the cross section scales like $P(b) \times b$, the major contribution to the cross sections comes from collisions with b between 1.0 and 3.0 Å for both H2T and endoperoxide channels. The absolute cross sections are 1.4 ± 0.7 Å^2 for the H2T channel (0.3 Å^2 from direct H2T and 1.1 Å^2 from hydroperoxide-mediated), and 0.9 ± 0.4 Å^2 for the endoperoxide channel, respectively. The trajectory calculated H2T cross section is considerably higher than the experimental measured cross section (0.2 Å^2) at this high energy. While the discrepancy may arise from the errors in the quantum chemistry method used to calculate forces as well as the absolute experimental uncertainty, we tentatively attribute the main discrepancy to the fact that the QCT method cannot simulate physical quenching of $^1O_2$, because trajectories are confined to the lowest energy singlet potential energy surface.

For the direct H2T channel, we also calculated energy distributions associated with the products. At $b = 0.1, 0.5, 1.0,$ 1.5, and 2.0 Å, the mean recoil energies $\langle E_{recoil} \rangle$ are 0.45, 0.32, 0.35, 0.46, and 1.23 eV, respectively; and the mean rotational energies $\langle E_{rot} \rangle$ are 0.61, 0.50, 0.75, 0.47, and 0.25 eV, respectively. The values of $\langle E_{recoil} \rangle$ increase with increasing b because large b collisions have more energy tied up in orbital motion and less along the line-of-centers for T $\rightarrow E_{vib}$ conversion. $\langle E_{rot} \rangle$ peaks in the middle of the reactive range of b, because orbital angular momentum and the collision moment arm increase with increasing b; however, the strength of the collisional interaction becomes weak at large values of b. The b-averaged values of $\langle E_{recoil} \rangle$ and $\langle E_{rot} \rangle$ are 0.70 and 0.46 eV; thus most of the available energy is partitioned to product vibrational energy.

Both the ab initio reaction coordinate for low collision energies and the trajectories at $E_{col} = 3.0$ eV show that the system can produce a mixture of endoperoxides. Based on complex forming efficiency and complex decay branching, RRKM theory predicts that, at lowest E_{col}, cross section for forming endoperoxides is up to 62 Å^2. In fact, formation of

endoperoxides overwhelms at $E_{col} \leq 0.1$ eV. This explains why the experimental H2T cross section drops off at $E_{col} = 0.1$ eV. However, none of these endoperoxides survives long enough to be detected in our instrument. The possibility of generating these intermediates raises an interesting dynamics question: Can these endoperoxides contribute to physical quenching of $^1O_2$? Several pieces of evidence support this idea. The reversible binding of $^1O_2$ to aromatic compounds by a [4 + 2] cyclization mechanism has been reported before.[81,82] The excitation energy of the triplet state of TyrH$^+$ is calculated to be 3.2 eV at B3LYP/6-31+G*, and the excitation energy of $^1O_2$ is 0.98 eV, so physical quenching (see eq 4 below) is energetically accessible at $E_{col} = 3.0$ eV. Generally, physical quenching arises from a charge-transfer induced intersystem crossing between ^{1}TyrH$^+$/$^1O_2$ and ^{3}TyrH^{+*}/$^3O_2$ within an exciplex.[4] It is a spin-allowed electronic energy transfer:[83]

$$TyrH^+ + {}^1O_2 \rightarrow [{}^{\delta+}TyrH^+ \cdots {}^1O_2{}^{\delta-}] \rightarrow$$
$$[{}^3TyrH^+ \cdots {}^3O_2] \rightarrow {}^3TyrH^+ + {}^3O_2 \quad (4)$$

We looked at the possibility of intracomplex charge transfer by examining the Mulliken charge on the O_2 moiety in the endoperoxides, and it turns out that the O_2 moiety has a negative charge more than -0.5. Therefore, endoperoxides (if formed) may be good candidates for mediating energy transfer at higher collision energies. At low collision energies, the electronic energy transfer is not energetically accessible, but physical quenching of $^1O_2$ could arise via electronic to vibrational energy transfer between reactants in endoperoxides.[4]

The issue of energy transfer during collisions raises a question about the use of QCT methods for trajectory simulations of $^1O_2$ reaction. There may exist two electronic states contributing to the lowest Born–Oppenheimer potential that the trajectory runs on, and the system may possibly go from ^{1}TyrH$^+$ + $^1O_2$ to ^{3}TyrH$^+$ + $^3O_2$ as reactants separate. There are two concerns here.[50,51] First, the QCT method does not allow nonadiabatic transitions at surface crossing seams. Such transitions would be important if the transition between the two states is abrupt. The fact that all trajectories have total energy conserved to the sum of individual electronic energies and rovibrational energies of ^{1}TyrH$^+$ and $^1O_2$ may imply that the transition, if existing, might be smooth. Another problem is this system is a likely a candidate for multiconfiguration wave functions. We tested this problem by running single point CASSCF(10,10) calculations for all geometries explored in the trajectories and found that the Hartree–Fock configuration is strongly dominant (coefficient >0.9), i.e., that multifunction wave functions should not be an issue in this system.

V. Conclusions

An electrospray-ionization, guided-ion beam tandem mass spectrometer was developed to examine the collision energy dependence of biomolecular ion interactions with molecules, including excited states. We are able to generate an intense and stable ion beam, with narrow kinetic energy spread and well thermalized ion internal energy distributions. We have measured the reaction of protonated tyrosine with the electronically excited singlet state of molecular oxygen ($^1O_2$, a$^1\Delta_g$), as a function of collision energy. Combined with electronic structure calculations and quasi-classical trajectory simulations, we have demonstrated that hydrogen peroxide is the product of this reaction and have provided a mechanism with considerable detail. At low energies, the reaction may be mediated by hydroperoxides, and at high

11260 *J. Phys. Chem. A, Vol. 113, No. 42, 2009*

Fang and Liu

energies a direct, concerted double H atom transfer also contributes. Competition with physical quenching is important and probably leads to the observed drop in reaction efficiency at E_{col} < 0.2 eV.

The current study may provide further understanding of tyrosine photooxidation susceptibility in biological systems and provide a basis for the development of models for photochemical transformations of tyrosine in atmospheric particles/drops. Assuming the pH of rainwater ranges from 3.5 to 5.7, a large fraction of tyrosine in atmospheric drops exist in the protonated structure, and reactions of tyrosine with photoformed $^1O_2$ account for most loss of tyrosine in atmosphere.[3,84]

References and Notes

(1) Davies, M. J. *Biochim. Biophys. Acta* **2005**, *1703*, 93.

(2) Palumbo, G. *Expert Opin. Drug Delivery* **2007**, *4*, 131.

(3) McGregor, K. G.; Anastasio, C. *Atmos. Environ.* **2001**, *35*, 1091.

(4) Wilkinson, F.; Helman, W. P.; Ross, A. B. *J. Phys. Chem. Ref. Data* **1995**, *24*, 663.

(5) Liu, J.; Zhang, F.; Zhao, Y.; Zhao, F.; Tang, Y.; Song, X. *Chin. Sci. Bull.* **1997**, *42*, 1624.

(6) Wright, A.; Bubb, W. A.; Hawkins, C. L.; Davies, M. J. *Photochem. Photobiol.* **2002**, *76*, 35.

(7) Criado, S.; Soltermann, A. T.; Marioli, J. M.; Garcia, N. A. *Photochem. Photobiol.* **1998**, *68*, 453.

(8) Yamashita, M.; Fenn, J. B. *J. Phys. Chem.* **1984**, *88*, 4451.

(9) Fenn, J. B.; Mann, M.; Meng, C. K.; Wong, S. F.; Whitehouse, C. M. *Science* **1989**, *246*, 64.

(10) Gerlich, D. Inhomogeneous RF fields: A versatile tool for the study of processes with slow ions In *State-Selected and State-to-State Ion− Molecule Reaction Dynamics. Part I. Experiment*; Ng, C. Y., Baer, M., Eds.; John Wiley & Sons, Inc.: New York, 1992; Vol. 82; pp 1.

(11) Marcus, R. A. *J. Chem. Phys.* **1952**, *20*, 359.

(12) Hoaglund-Hyzer, C. S.; Counterman, A. E.; Clemmer, D. E. *Chem. Rev.* **1999**, *99*, 3037.

(13) Kaltashov, I. A.; Eyles, S. J. *Mass Spectrometry in Biophysics: Conformation and Dynamics of Biomolecules*; John Wiley & Sons: Hoboken, NJ, 2005.

(14) Barran, P. E.; Polfer, N. C.; Campopiano, D. J.; Clarke, D. J.; Langridge-Smith, P. R. R.; Langley, R. J.; Govan, J. R. W.; Maxwell, A.; Dorin, J. R.; Millar, R. P.; Bowers, M. T. *Int. J. Mass Spectrom.* **2005**, *240*, 273.

(15) Wolynes, P. G. *Proc. Natl. Acad. Sci. U.S.A.* **1995**, *92*, 2426.

(16) Bonneet, R. *Chemical Aspects of Photodynamic Therapy*; Gordon and Breach Science Publishers: Singapore, 2000.

(17) Chiu, Y.-H.; Fu, H.; Huang, J.-T.; Anderson, S. L. *J. Chem. Phys.* **1995**, *102*, 1199.

(18) Moision, R. M.; Armentrout, P. B. *J. Am. Soc. Mass Spectrom.* **2007**, *18*, 1124.

(19) DeTuri, V. F.; Hintz, P. A.; Ervin, K. M. *J. Phys. Chem.* **1997**, *101*, 5969.

(20) Chowdhury, S. K.; katta, V.; Chait, B. T. *Rapid Commun. Mass Spectrom.* **1990**, *4*, 81.

(21) Kim, T.; Tang, K.; Udseth, H. R.; Smith, R. D. *Anal. Chem.* **2001**, *73*, 4162.

(22) Tang, K.; Tolmachev, A. V.; Nikolaev, E.; Zhang, R.; Belov, M. E.; Udseth, H. R.; Smith, R. D. *Anal. Chem.* **2002**, *74*, 5431.

(23) Jones, R. M.; Anderson, S. L. *Rev. Sci. Instrum.* **2000**, *71*, 4335.

(24) Krutchinsky, A. N.; Chernushevich, I. V.; Spicer, V. L.; Ens, W.; Standing, K. G. *J. Am. Soc. Mass Spectrom.* **1998**, *9*, 569.

(25) Douglas, D. J.; French, J. B. *J. Am. Mass Spectrom.* **1992**, *3*, 398.

(26) *LabVIEW*; ver. 8.5; National Instruments Corporation: Austin, TX, 2007.

(27) Ervin, K. M.; Armentrout, P. B. *J. Chem. Phys.* **1985**, *83*, 166.

(28) Moision, R. M.; Armentrout, P. B. *J. Phys. Chem. A* **2006**, *110*, 3933.

(29) Liu, J.; Van Devener, B.; Anderson, S. L. *J. Chem. Phys.* **2002**, *116*, 5530.

(30) Armentrout, P. B. *Int. J. Mass Spectrom.* **2000**, *200*, 219.

(31) Sowa-Resat, M. B.; Hintz, P. A.; Anderson, S. L. *J. Phys. Chem.* **1995**, *99*, 10736.

(32) Levine, R. D.; Bernstein, R. B. *Molecular Reaction Dynamics and Chemical Reactivity*; Oxford University Press: New York, 1987.

(33) Foresman, J. B.; Frisch, A. *Exploring Chemistry with Electronic Structure Methods*, 2nd ed.; Gaussian, Inc: Pittsburgh, PA, 2000.

(34) Rodgers, M. T.; Ervin, K. M.; Armentrout, P. B. *J. Chem. Phys.* **1997**, *106*, 4419.

(35) Zhu, L.; Hase, W. L. *A General RRKM Program(QCPE 644), Quantum Chemistry Program Exchange*; Chemistry Department, University of Indiana: Bloomington, 1993.

(36) Ogryzlo, E. A. Gaseous Singlet Oxygen In *Singlet Oxygen*; Wasserman, H. H., Murray, R. W., Eds.; Academic Press, Inc.: New York, 1979; pp 35.

(37) Savin, Y. V.; Goryachev, L. V.; Adamenkov, Y. A.; Rakhimova, T. V.; Mankelevich, Y. A.; Popov, N. A.; Adamenkov, A. A.; Egorov, V. V.; Ilyin, S. P.; Kolobyanin, Y. V.; Kudryashov, E. A.; Rogozhnikov, G. S.; Vyskubenko, B. A. *J. Phys. D: Appl. Phys.* **2004**, *37*, 3121.

(38) Fehsenfeld, F. C.; Evenson, K. M.; Broida, H. P. *Rev. Sci. Instrum.* **1965**, *36*, 294.

(39) Troe, J. *Chem. Phys. Lett.* **1985**, *122*, 425.

(40) Popović, S.; Rašković, M.; Kuo, S. P.; Vušković, L. *J. Phys.: Conf. Ser.* **2007**, *86*, 012013.

(41) Baeva, M.; Luo, X.; Pfelzer, B.; Repsilber, T.; Uhlenbusch, J. *Plasma Sources Sci. Technol.* **2000**, *9*, 128.

(42) Melton, D. W.; Lowe, B. F.; Perram, G. P.; Roh, W. B. *J. Chem. Phys.* **1991**, *95*, 4933.

(43) Midey, A.; Dotan, I.; Lee, S.; Rawlins, W. T.; Johnson, M. A.; Viggiano, A. A. *J. Phys. Chem. A* **2007**, *11*, 5218.

(44) Duo, L.; Cui, T.; Wang, Z.; Chen, W.; Yang, B.; Sang, F. *J. Phys. Chem. A* **2001**, *105*, 281.

(45) Collins, R. J.; Husain, D.; Donovan, R. J. *J. Chem. Soc., Faraday Trans. 2: Mol. Chem. Phys.* **1973**, *69*, 145.

(46) Frisch, M. J.; Trucks, G. W.; Schlegel, H. B.; Scuseria, G. E.; Robb, M. A.; Cheeseman, J. R.; Montgomery, J. A., Jr.; Vreven, T.; Kudin, K. N.; Burant, J. C.; Millam, J. M.; Iyengar, S. S.; Tomasi, J.; Barone, V.; Mennucci, B.; Cossi, M.; Scalmani, G.; Rega, N.; Petersson, G. A.; Nakatsuji, H.; Hada, M.; Ehara, M.; Toyota, K.; Fukuda, R.; Hasegawa, J.; Ishida, M.; Nakajima, T.; Honda, Y.; Kitao, O.; Nakai, H.; Klene, M.; Li, X.; Knox, J. E.; Hratchian, H. P.; Cross, J. B.; Adamo, C.; Jaramillo, J.; Gomperts, R.; Stratmann, R. E.; Yazyev, O.; Austin, A. J.; Cammi, R.; Pomelli, C.; Ochterski, J. W.; Ayala, P. Y.; Morokuma, K.; Voth, G. A.; Salvador, P.; Dannenberg, J. J.; Zakrzewski, V. G.; Dapprich, S.; Daniels, A. D.; Strain, M. C.; Farkas, O.; Malick, D. K.; Rabuck, A. D.; Raghavachari, K.; Foresman, J. B.; Ortiz, J. V.; Cui, Q.; Baboul, A. G.; Clifford, S.; Cioslowski, J.; Stefanov, B. B.; Liu, G.; Liashenko, A.; Piskorz, P.; Komaromi, I.; Martin, R. L.; Fox, D. J.; Keith, T.; Al-Laham, M. A.; Peng, C. Y.; Nanayakkara, A.; Challacombe, M.; Gill, P. M. W.; Johnson, B.; Chen, W.; Wong, M. W.; Gonzalez, C.; Pople, J. A. *Gaussian 03*, revision C.01; Gaussian, Inc.: Wallingford, CT, 2004.

(47) Hase, W. L.; Bolton, K.; de Sainte Claire, P.; Duchovic, R. J.; Hu, X.; Komornicki, A.; Li, G.; Lim, K.; Lu, D.; Peslherbe, G. H.; Song, K.; Swamy, K. N.; Vande Linde, S. R.; Varandas, A.; Wang, H.; Wolf, R. J. VENUS99: A general chemical dynamics computer program, 1999.

(48) Bakken, V.; Millam, J. M.; Schlegel, H. B. *J. Chem. Phys.* **1999**, *111*, 8773.

(49) Bacskay, G. B. *Chem. Phys.* **1981**, *61*, 385.

(50) Liu, J.; Uselman, B.; Boyle, J.; Anderson, S. L. *J. Chem. Phys.* **2006**, *125*, 133115.

(51) Boyle, J. M.; Liu, J.; L.Anderson, S. *J. Phys. Chem. A* **2009**, *113*, 3911.

(52) Laaksonen, L. *gOpenMol*, 2.2 ed.; available at www.csc.fi/gopenmol/, Espoo, Finland, 2002.

(53) Liu, J.; Song, K.; Hase, W. L.; Anderson, S. L. *J. Chem. Phys.* **2003**, *119*, 3040.

(54) Liu, J.; Song, K.; Hase, W. L.; Anderson, S. L. *J. Am. Chem. Soc.* **2004**, *126*, 8602.

(55) Liu, J.; Song, K.; Hase, W. L.; Anderson, S. L. *J. Phys. Chem. A* **2005**, *109*, 11376.

(56) Untch, A.; Schinke, R.; Cotting, R.; Huber, J. R. *J. Chem. Phys.* **1993**, *99*, 9553.

(57) Miller, W. H. *J. Chem. Soc., Faraday Trans.* **1997**, *93*, 685.

(58) Aribi, H. E.; Orlova, G.; Hopkinson, A. C.; Siu, K. W. M. *J. Phys. Chem. A* **2004**, *108*, 3844.

(59) Zhao, J.; Shoeib, T.; Siu, K. W. M.; Hopkinson, A. C. *Int. J. Mass Spectrom.* **2006**, *255−256*, 265.

(60) Lioe, H.; O'Hair, R. A. J. *Anal. Bioanal. Chem.* **2007**, *389*, 1429.

(61) Kotiaho, T.; Eberlin, M. N.; Vainiotalo, P.; Kostiainen, R. *J. Am. Soc. Mass Spectrom.* **2000**, *11*, 526.

(62) Lloyd, J. A.; Spraggins, J. M.; Johnston, M. V.; Laskin, J. *J. Am. Soc. Mass Spectrom.* **2006**, *17*, 1289.

(63) Buettner, G. R.; Need, M. J. *Cancer Lett.* **1985**, *25*, 297.

(64) Kramarenko, G. G.; Hummel, S. G.; Martin, S. M.; Buettner, G. R. *Photochem. Photobiol.* **2006**, *82*, 1634.

(65) , P. W., Jr.; Jones, L. H.; Wentworth, A. D.; Zhu, X.; Larsen, N. A.; Wilson, I. A.; Xu, X.; Goddard, W. A., III; Janda, K. D.; Eschenmoser, A.; Lerner1, R. A. *Science* **2001**, *293*, 1806.

(66) Eyet, N.; Midey, A.; Bierbaum, V. M.; Viggiano, A. A. *J. Phys. Chem. A* **2009**, DOI: 10.1021/jp904235m.

(67) Lioe, H.; O'Hair, R. A. J. *Org. Biomol. Chem.* **2005**, *3*, 3618.

(68) Maksik, Z. B.; Kovacevic, B. *Chem. Phys. Lett.* **1999**, *307*, 497.

(69) Cohen, R.; Brauer, B.; Nir, E.; Grace, L.; de Vries, M. S. *J. Phys. Chem. A* **2000**, *104*, 6351.

(70) Carreo, M. C.; Gonzalez-Lopez, M.; Urbano, A. *Angew. Chem., Int. Ed.* **2006**, *45*, 2737.

(71) Chen, Y.-Z.; Wu, L.-Z.; Peng, M.-L.; Zhang, D.; Zhang, L.-P.; Tung, C.-H. *Tetrahedron* **2006**, *62*, 10688.

(72) Morgan, P. E.; Dean, R. T.; Davies, M. J. *Free Radical Biol. Med.* **2008**, *36*, 484.

(73) Gracanin, M.; Hawkins, C. L.; Pattison, D. I.; Davies, M. J. *Free Radical Biol. Med.* **2009**, *47*, 92.

(74) Liu, J.; Devener, B. V.; Anderson, S. L. *J. Chem. Phys.* **2002**, *117*, 8292.

(75) Bertolotti, S. G.; Garcia, N. A.; Arguello, G. A. *J. Photochem. Photobiol. B: Biol.* **1991**, *10*, 57.

(76) Criado, S.; Soltermann, A. T.; Garcia, N. A. *Amino Acids* **1995**, *8*, 367.

(77) Criado, S.; Marioli, J. M.; Allegretti, P. E.; Furlong, J.; Nieto, F. J. R.; Martire, D. O.; Garcia, N. A. *J. Photochem. Photobiol. B: Biol.* **2001**, *65*, 74.

(78) Posadaz, A.; Biasutti, A.; Casale, C.; Sanz, J.; Amat-Guerri, F.; Garcia, N. A. *Photochem. Photobiol.* **2004**, *80*, 132.

(79) Endo, K.; Seya, K.; Hikino, H. *J. Chem. Soc., Chem. Commun.* **1998**, *14*, 934.

(80) Press, W. H.; Teukolsky, S. A.; Vetterling, W. T.; Flannery, B. P. *Numerical Recipies in C. The Art of Scientific Computing*, 2nd ed.; Cambridge University Press: Cambridge, U.K., 1992.

(81) Moureu, C.; Dufraisse, C.; Dean, P. M. *C. R. Acad. Sci.* **1926**, *182*, 1584.

(82) Martinez, G. R.; Garcia, F.; Catalani, L. H.; Cadet, J.; Oliveira, M. C. B.; Ronsein, G. E.; Miyamoto, S.; Medeiros, M. H. G.; Masciod, P. D. *Tetrahedron* **2006**, *62*, 10762.

(83) Farmilo, A.; Wilkinson, F. *Photochem. Photobiol.* **1973**, *18*, 447.

(84) Anastasio, C.; McGregor, K. G. *Atmos. Environ.* **2001**, *35*, 1079.